

DARK MATTER IN DISEQUILIBRIUM: THE LOCAL VELOCITY DISTRIBUTION FROM SDSS-*GAIA*

LINA NECIB

Walter Burke Institute for Theoretical Physics, California Institute of Technology, Pasadena, CA 91125, USA

MARIANGELA LISANTI

Department of Physics, Princeton University, Princeton, NJ 08544, USA

VASILY BELOKUROV

Institute of Astronomy, University of Cambridge, Madingley Road, Cambridge CB3 0HA, UK
 and

Center for Computational Astrophysics, Flatiron Institute, 162 5th Avenue, New York, NY 10010, USA

ABSTRACT

We use the distribution of accreted stars in SDSS-*Gaia* DR2 to demonstrate that the local dark matter halo may not be in equilibrium and that a non-trivial fraction is in substructure. Using a mixture likelihood analysis, we separate the contributions of an old, isotropic stellar halo and a younger anisotropic population. The latter dominates and is uniform within Galactocentric radii of 7.5–10 kpc and $|z| > 2.5$ kpc. It can be explained as the tidal debris of a disrupted massive satellite on a highly radial orbit, and is consistent with mounting evidence from recent studies. Simulations that track the tidal debris from such mergers find that the dark matter traces the kinematics of its stellar counterpart. If so, our results indicate that the majority of the local dark matter that is sourced by luminous satellites is in kinematic substructure referred to as debris flow. These results challenge the Standard Halo Model, which is highly discrepant with the distribution recovered from the stellar data, and have important ramifications for the interpretation of direct detection experiments.

1. INTRODUCTION

The motions of nearby stars have proven invaluable in the study of the local dark matter (DM) distribution, starting from the work of Kapteyn (Kapteyn 1922), Jeans (Jeans 1922), and Oort (Oort 1932). As the mapping of stellar velocities has dramatically improved with surveys such as Hipparcos (ESA 1997), the Sloan Digital Sky Survey (SDSS) (Ahn et al. 2012), and the RAdial Velocity Experiment (Kunder et al. 2017), the measurement of the local DM density has become a science (Read 2014). In contrast, the DM velocity distribution has remained relatively unexplored. In this work, we use data from the second *Gaia* data release (Gaia Collaboration et al. 2016, 2018), cross-matched with SDSS, to characterize the local population of accreted stars and infer properties of the DM velocity distribution.

In the Λ CDM paradigm, the Milky Way halo is built from the mergers of smaller satellite galaxies (White &

Rees 1978). As these galaxies fall into the Milky Way, they experience strong tidal forces that gradually tear them apart. In the initial stages of disruption, the DM in the outskirts of the satellite is stripped away, but as the galaxy is slowly eaten down, its more tightly bound stars and DM are also removed. This tidal debris litters the Milky Way, a fossil remnant of the Galaxy’s accretion history.

DM that accreted early has time to virialize with the host galaxy. We can thus imagine that it forms an isotropic isothermal halo (Ostriker et al. 1974; Bahcall & Soneira 1980; Caldwell & Ostriker 1981) with a mass distribution that is consistent with a flat rotation curve (Blitz 1979; Burton & Gordon 1978; Clemens 1985; Knapp et al. 1985; Fich et al. 1989; Pont et al. 1994). Self-consistently, the local DM velocities follow a Maxwell-Boltzmann distribution (Drukier et al. 1986; Freese et al. 1988). This scenario is often referred to as the Standard Halo Model.

More recent mergers, however, can leave residual

structures in the DM phase-space distribution. For example, the debris from the youngest mergers may be in position and velocity substructure. Referred to as tidal streams, these cold phase-space features tend to trace fragments of a progenitor’s orbit (Zemp et al. 2009; Vogelsberger et al. 2009; Diemand et al. 2008; Kuhlen et al. 2010; Maciejewski et al. 2011; Vogelsberger & White 2011; Elahi et al. 2011). With time, the tidal debris becomes increasingly more mixed. In this process, any velocity features typically persist longer than spatial ones (Helmi & White 1999). The resulting kinematic substructure, referred to as debris flow, may consist of many overlapping streams, shells or plumes from the debris of one or more satellites that have made several orbits before dissolving (Lisanti & Spergel 2012; Kuhlen et al. 2012).

N -body simulations are an invaluable tool in exploring the range of DM distributions possible in Milky Way-like galaxies. They have demonstrated, for example, that the Solar neighborhood could have been built from a wide variety of accretion histories (Diemand et al. 2007; Wang et al. 2011). DM-only simulations find fairly marked deviations from the Maxwell-Boltzmann assumption, especially on the high-end tail of the velocity distribution (Vogelsberger et al. 2009; March-Russell et al. 2009; Fairbairn & Schwetz 2009; Kuhlen et al. 2010; Mao et al. 2013). Simulations that also model the baryonic physics typically exhibit closer alignment with the Maxwell Boltzmann, although significant scatter is observed between them (Ling et al. 2010; Pillepich et al. 2014; Bozorgnia et al. 2016; Kelso et al. 2016; Sloane et al. 2016; Bozorgnia & Bertone 2017).

Ultimately, we would like to determine the local DM distribution from observations. One possibility is to use the motion of stars to constrain the local gravitational potential (or density) and to subsequently infer the velocity distribution using Jeans Theorem. A variety of proposals of this nature have been made (Hansen & Moore 2006; Chaudhury et al. 2010; Lisanti et al. 2011; Bhattacharjee et al. 2013; Catena & Ullio 2012; Bozorgnia et al. 2013; Fornasa & Green 2014; Mandal et al. 2018), but they typically rely on the assumption that the DM is isotropic and/or in equilibrium, either of which may be violated depending on the Milky Way’s accretion history.

An alternative proposal is to identify populations of stars that share the same kinematics as the DM. These are stars that were also accreted onto the Milky Way from merging satellites. As such, they typically have distinctive kinematic and chemical properties compared to the population that is born in the Galaxy. Using accreted stars as direct kinematic tracers for the DM is beneficial because it makes no assumption about steady state. The potential downside to this approach is that

it does not account for DM that originates from non-luminous satellites or that was accreted diffusely.

Numerical simulations have demonstrated excellent correspondence between the DM and accreted stars. Herzog-Arbeitman et al. (2017a) recently showed that the oldest and most metal-poor stars in the halo trace the velocities of the virialized DM using the *Eris* hydrodynamic N -body simulation. Stellar substructure in the form of debris flow also traces similar kinematic features in the DM distribution, as was demonstrated using the *Via Lactea* simulation (Lisanti et al. 2015). As this substructure arises from more recent accretion events than the virialized component, it may be associated with more metal-rich stars.

These arguments motivate a close study of the local accreted stellar population as a means of characterizing the DM distribution. Recent observations have begun to change our understanding of the stellar halo, disfavoring the viewpoint that a large fraction was born *in-situ* from stars that were kicked up from the Galactic disk (Helmi 2008). In contrast, evidence has been building for a two-component model that consists of an isotropic population from old accretion events, and an anisotropic population from a more recent—and quite significant—merger (Belokurov et al. 2018a; Deason et al. 2018; Myeong et al. 2018; Helmi et al. 2018; Lancaster et al. 2018). In this picture, the majority of the local stellar halo originates from this one merger, which also deposits DM. This work presents the first modeling of the velocity and metallicities of the stars accreted in this event, providing clues about the corresponding DM debris as well.

The second *Gaia* data release (DR2) presents a unique opportunity to study the kinematics of this accreted population. Cross-matching *Gaia* DR2 with SDSS yields metallicities for 193,162 of its stars. This dataset allows us to characterize the velocity distribution of stars with metallicities down to $[\text{Fe}/\text{H}] \sim -3$ between Galactocentric radii of 7.5–10 kpc and $|z| > 2.5$ kpc. We build a model that successfully describes the observations over the full range of metallicities and velocities. As we will argue, the properties of the local stellar distribution suggest that a substantial fraction of the local DM is in substructure called debris flow. The assumption of local equilibrium is therefore violated, challenging the Standard Halo Model.

Characterizing the DM velocity distribution is critical for interpreting results of direct detection experiments, which search for the recoils of nuclei from a collision with a DM particle—see Jungman et al. (1996); Freese et al. (2013) for reviews. The rate of such scattering interactions depends on the DM speed upon collision. Indeed, for certain DM speeds and/or models the velocity distribution can make the difference between observing a sig-

nal or seeing nothing at all. The characterization of the DM velocity distribution function is one of the largest sources of uncertainty in the interpretation of such experimental results (Del Nobile 2014; Green 2017). If the majority of the local DM is indeed in disequilibrium, it could potentially change the landscape of exclusion limits on DM masses and scattering cross sections.

Our paper is organized as follows. Sec. 2 describes the data preparation and likelihood procedure used in the study. Sec. 3 presents the results of the SDSS-*Gaia* DR2 analysis, and describes the characteristics of the disk, halo, and substructure stars that we identify. Sec. 4 discusses the implications of this stellar substructure for DM detection. Figs. 8 and 9 summarize the impact on experimental limits for spin-independent interactions. We conclude in Sec. 5. The Appendix includes supplementary material that further substantiates the results presented in the main text. Interpolations of the heliocentric velocity distribution, which can be used to calculate DM scattering rates, are provided at the following `github` repository https://linoush.github.io/DM_Velocity_Distribution/.

2. ANALYSIS METHODOLOGY

2.1. Data Selection

In this analysis, we use the SDSS DR9 (Ahn et al. 2012) dataset, cross-matched to *Gaia* DR2 (Gaia Collaboration et al. 2018). The cross-match was performed inside the Whole Sky Data Base (WSDB), an archive providing SQL access to catalogs from all major wide-area surveys. In particular, we utilized Q3C, spatial indexing and cross-matching plug-in (Koposov & Bartunov 2006) to select the nearest SDSS neighbor for each *Gaia* source within $1''$ aperture, while taking into account the proper motion of all objects as well as the time difference between the observations. The combination of the two datasets allows us to take advantage of the large number of halo stars in the SDSS spectroscopic dataset, while simultaneously using the unprecedented accuracies of the proper motions provided by the *Gaia* survey. From the SDSS catalog, we select Main Sequence stars that satisfy: $|b| > 10^\circ$, $A_g < 0.5$ mag, $\sigma_{RV} < 50$ km/s, $S/N > 10$, $3.5 < \log(g) < 5$, $0.2 < g - r < 0.8$, $0.2 < g - i < 4$, $4500 < T_{\text{eff}} < 8000$ K, and $15 < r < 19.5$. All stellar magnitudes are dereddened using the maps of Schlegel et al. (1998).

Distances to these predominantly Main Sequence stars are calculated using equations (A2), (A3), and (A7) of Ivezić et al. (2008). Recently, the validity of this photometric parallax calibration was verified by Deason et al. (2018) for a subset of stars with accurate *Gaia* DR2 parallaxes. We have also confirmed that the fractional errors on the distance as derived from the paral-

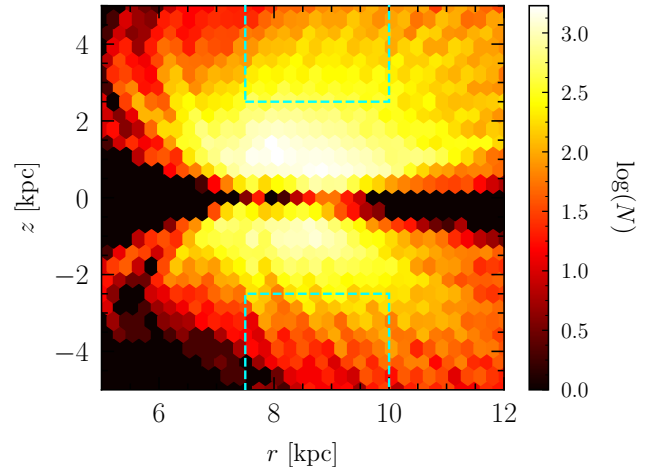


Figure 1. The spatial distribution of the SDSS-*Gaia* DR2 sample in terms of Galactocentric radius, r , and vertical distance from the Galactic plane, z . We characterized the disk, halo, and substructure populations in regions within the dashed aqua box, which spans $r \in [7.5, 10.0]$ kpc and $|z| > 2.5$ kpc.

axes are consistently larger than those derived using the photometric parallax. The celestial coordinates, heliocentric distances, proper motions and radial velocities are then used to calculate stellar velocity components in spherical polar coordinates. We marginalize over the Local Standard of Rest value assuming that it is described by a Gaussian with a center at 238 km/s and a dispersion of 9 km/s (Schönrich 2012). The components of the Solar peculiar motion are those presented in Coşkunoglu et al. (2011). The measured parameters’ uncertainties—including covariances in the proper motion components—are then propagated using Monte-Carlo sampling to obtain estimates of the uncertainties in the spherical velocity components (see Belokurov et al. 2018b, for details). For the analysis described in the Sections below, each star’s Monte Carlo samples are modeled with a Gaussian distribution to obtain the full covariance matrix.

There are no strong reasons to believe that the SDSS spectroscopic sample of Main Sequence stars used in our analysis suffers from any appreciable kinematic bias. However, as the sample uses a mixture of SDSS target categories, a moderate metallicity bias towards more metal-poor stars is expected (see Yanny et al. 2009, for details). We also repeated our benchmark analysis selecting only F/G stars, which are known to have no biases either in metallicity or kinematics. This reduces the sample size substantially, increasing the uncertainties on the recovered fit parameters. However, the overall results—most importantly the fractional contribution of

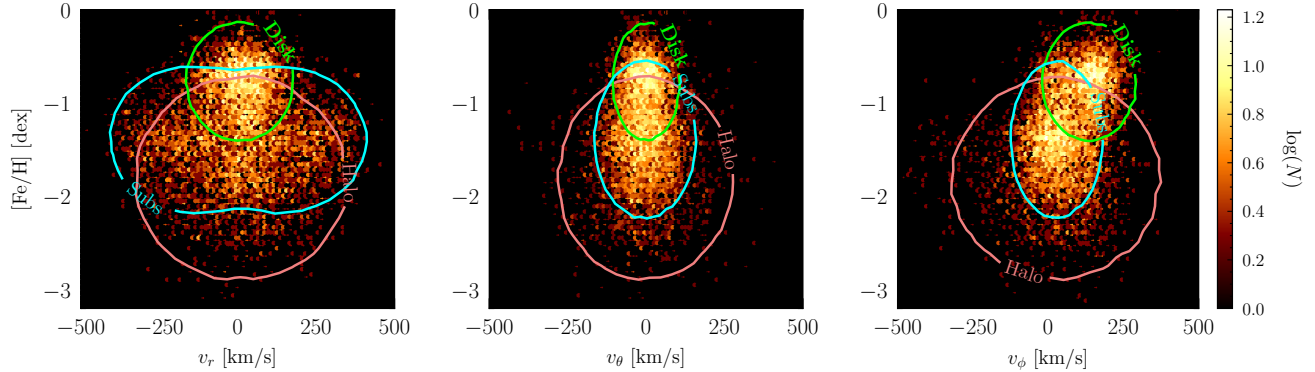


Figure 2. Chemo-dynamic distribution of stars in the SDSS-*Gaia* DR2 sample within $r \in [7.5, 8.5]$ kpc and $|z| > 2.5$ kpc. The panels show how the distributions vary in iron abundance $[\text{Fe}/\text{H}]$ and the spherical Galactocentric radial coordinates v_r (left), v_θ (middle), and v_ϕ (right). The disk population is pronounced at $[\text{Fe}/\text{H}] \sim -0.8$ and a nearly isotropic halo population is apparent at $[\text{Fe}/\text{H}] \lesssim -1.8$. A highly radial population at $[\text{Fe}/\text{H}] \sim -1.4$ constitutes a large fraction of the sample and is an example of kinematic substructure. The 95% contours of the posterior distributions recovered from the likelihood analysis are also shown (see Sec. 2.3); the disk, halo, and substructure best-fits are shown in green, pink, and blue, respectively.

the stellar components—remain essentially unchanged, within uncertainties.

Fig. 1 shows the spatial distribution of stellar counts in SDSS-*Gaia* DR2, as a function of Galactocentric radius, r , and vertical distance from the Galactic plane, z .

2.2. Model Motivation

Fig. 2 shows the distribution of the spherical velocity components as a function of stellar metallicity¹ for the SDSS-*Gaia* DR2 subsample within $r \in [7.5, 8.5]$ kpc and $|z| > 2.5$ kpc. Several features are apparent by visual inspection. First is the disk population, which is centered at $[\text{Fe}/\text{H}] \sim -0.8$, $v_{r,\theta} \sim 0$ km/s, and $v_\phi \sim 130$ km/s. Second, is a population with $[\text{Fe}/\text{H}] \sim -1.4$ with large radial anisotropy. Third, is a population that extends down to $[\text{Fe}/\text{H}] \lesssim -1.8$ with nearly isotropic velocities.²

In this work, we will refer to the second population as ‘substructure’ and the third population as the ‘halo.’ We are envisioning that both originate from the disruption of accreted satellites in the Milky Way. What we refer to as the ‘halo’ is intended to encapsulate the tidal debris from the oldest mergers, which will typically be the most metal-poor and fully well-mixed in phase space. What we call ‘substructure’ constitutes tidal debris that is not

fully phase mixed; such a component may exhibit interesting features in spatial and/or velocity coordinates, such as streams or debris flow. The prefix ‘sub-’ suggests that this population is less dominant than the halo population; we adopt this terminology as it is standard in the DM literature, but make no assumptions on its relative dominance in our study.

Evidence has been building for a multi-component inner stellar halo that is dominated by the tidal debris of one massive merger (Deason et al. 2015; Fiorentino et al. 2015; Belokurov et al. 2018a; Helmi et al. 2018). The large radial anisotropy of the stars with $[\text{Fe}/\text{H}] \gtrsim -1.7$ in Fig. 2 was first identified using the SDSS-*Gaia* DR1 sample (Belokurov et al. 2018b).³ This work noted that the ‘sausage’-like feature in the data appears to be non-Gaussian and estimated its contribution to be $\sim 66\%$ of the non-disk population over the full SDSS footprint. They found that the radial anisotropy of the sample drops markedly at $[\text{Fe}/\text{H}] \lesssim -1.7$, suggesting that a separate isotropic and metal-poor population is also present. It is unlikely that the radial and isotropic populations originated in the Milky Way as their iron abundances are in-line with those observed in Milky Way dwarf spheroidal galaxies (Venn et al. 2004) and their velocities are distinct from disk stars.

Recent work using local Main Sequence stars from SDSS-*Gaia* DR2 as well as a separate sample of more distant Blue Horizontal Branch stars demonstrated that the orbits of the most highly eccentric stars share a com-

¹ In particular, we use the iron abundance, $[\text{Fe}/\text{H}]$, which is defined as

$$[\text{Fe}/\text{H}] = \log_{10}(N_{\text{Fe}}/N_{\text{H}}) - \log_{10}(N_{\text{Fe}}/N_{\text{H}})_{\odot},$$

where N_i is the number density of the element i .

² We also note a small cluster of stars at $[\text{Fe}/\text{H}] \sim -1.5$ and $v_\phi < -200$ km/s. These stars may or may not be part of a distinct population; because they constitute only 0.5% of the total sample, we will not focus on them in this work. They are primarily flagged as ‘halo’ stars in the likelihood study.

³ Note that we define ϕ and θ as the azimuthal and polar directions, respectively. This is the opposite of the convention used in Belokurov et al. (2018b).

Parameter	Type	Priors		
		Disk	Halo	Sub
μ_r	linear	$[-70, 70]$	$[-70, 70]$	$[0, 250]$
μ_θ	linear	$[-70, 70]$	$[-70, 70]$	$[-70, 70]$
μ_ϕ	linear	$[0, 300]$	$[-70, 70]$	$[-70, 70]$
$\sigma_{r,\theta,\phi}$	linear	$[0, 200]$	$[0, 200]$	$[0, 200]$
$\rho_{r\theta, r\phi, \theta\phi}$	linear	$[-1, 1]$	$[-1, 1]$	$[-1, 1]$
$\mu_{[\text{Fe}/\text{H}]}$	linear	$[-1.5, 0.5]$	$[-3, -1]$	$[-3, -1]$
$\sigma_{[\text{Fe}/\text{H}]}$	linear	$[0, 2]$	$[0, 2]$	$[0, 2]$
Q	linear	—	$[0, 1]$	$[0, 1]$

Table 1. Parameters and associated prior types/ranges for the disk, halo, and substructure populations.

mon apocenter at $r \sim 20$ kpc (Deason et al. 2018). This radius is coincident with the observed break in the Milky Way’s stellar density distribution (Deason et al. 2013), suggesting that the radial stellar population is the tidal debris of a recent and large merger that dominates the inner halo. This hypothesis is further supported by simulations showing that shells can form near the apocenter of such orbits, creating density breaks (Johnston et al. 2008; Cooper et al. 2010).

If the radial substructure is indeed associated with a large merger, one might expect that globular clusters were also stripped from the satellite progenitor as it was disrupted. Indeed, a number of globular clusters on highly radial orbits were recently identified that may be associated with the large merger(s) causing the sausage-like feature in the SDSS-*Gaia* data (Myeong et al. 2018). The number of these clusters suggests a total progenitor mass of $\sim 10^{10} M_\odot$; their tracks in age-metallicity space bound the maximum infall redshift less than ~ 3 .

These new results have direct implications for the local DM distribution. Previous work demonstrated that the virialized DM component is traced by the most metal-poor stars in the Milky Way—this corresponds to the population that we refer to as the halo here (Herzog-Arbeitman et al. 2017a). Additionally, the kinematic substructure observed in the data is highly reminiscent of debris flow (Lisanti & Spergel 2012; Kuhlen et al. 2012). Indeed, a study of the stellar halo in *Via Lactea* (where star particles were painted onto the most bound DM particles in subhalos) found precisely the same kind of radial substructure becoming apparent in the SDSS-*Gaia* data, and that the kinematics of the accreted stars correlate with that of the DM debris (Lisanti et al. 2015). Therefore, if we want to infer the kinematic properties of the local DM, we will need to model the velocities of the halo and substructure populations.

2.3. Likelihood Procedure

To isolate the accreted stellar population, we can place a hard upper cut-off on the metallicity of the sample. The downside to this conservative approach is that it ignores the high-metallicity tail of the accreted stellar distribution that overlaps with disk stars. For this reason, we use a mixture model analysis to statistically identify the individual populations of accreted stars over the full metallicity range of the sample.

Each star, labeled by the index i , is associated with a set of observable quantities such as its velocity and metallicity, $O_i = (\mathbf{v}_i, [\text{Fe}/\text{H}]_i)$, as well as the variance for each. We assign each star a flag $j = d, h, s$ that designates whether it belongs to the disk, halo, or substructure population, respectively. The likelihood of observing O_i for a disk star is

$$p_d(O_i | \theta) = \mathcal{N}(\mathbf{v}_i | \boldsymbol{\mu}^d, \boldsymbol{\Sigma}_i^d) \mathcal{N}([\text{Fe}/\text{H}]_i | \mu_{[\text{Fe}/\text{H}]}^d, \sigma_{[\text{Fe}/\text{H}]}^d), \quad (1)$$

where θ is the set of free parameters and \mathcal{N} denotes the normal distribution. The set θ includes the velocity distribution mean $\boldsymbol{\mu}^d$ and covariance matrix $\boldsymbol{\Sigma}_i^d$, as well as the metallicity distribution mean $\mu_{[\text{Fe}/\text{H}]}^d$ and dispersion $\sigma_{[\text{Fe}/\text{H}]}^d$. The covariance matrix depends on the individual velocity dispersions $\sigma_{r,\theta,\phi}$ as well as the correlation coefficients $\rho_{r\theta}, \rho_{r\phi}, \rho_{\theta\phi}$. Note that the velocity covariance matrix and the metallicity dispersion vary between stars because the observed covariance depends on the true value and the measurement error—specifically, $\boldsymbol{\Sigma}_{\text{obs}} = \boldsymbol{\Sigma}_{\text{true}} + \boldsymbol{\Sigma}_{\text{err}}$. There are eleven parameters associated with this model. The likelihood for a halo star is also given by (1), except with $d \rightarrow h$, and thus comes with an additional eleven parameters.

Modeling the substructure population is more challenging as initial evidence suggests that its radial velocities are non-Gaussian (Belokurov et al. 2018b). Therefore, we assume that the velocities are a sum of two multivariate normal distributions with equivalent parameters, except for equal and opposite mean in v_r :

$$p_s(O_i | \theta) = \frac{1}{2} [\mathcal{N}(\mathbf{v}_i | \boldsymbol{\mu}^s, \boldsymbol{\Sigma}_i^s) + \mathcal{N}(\mathbf{v}_i | \boldsymbol{\mu}^s, \boldsymbol{\Sigma}_i^s)] \times \mathcal{N}([\text{Fe}/\text{H}]_i | \mu_{[\text{Fe}/\text{H}]}^s, \sigma_{[\text{Fe}/\text{H}]}^s), \quad (2)$$

where $\boldsymbol{\mu}^s = (-\mu_r, \mu_\theta, \mu_\phi)^s$. This model can vary over unimodal and bimodal distributions in v_r . For example, when $\mu_r^s \rightarrow 0$, (2) approaches a single Gaussian distribution peaked at zero. In the limit where $\mu_r^s \gg \sigma_r^s$ and $\mu_r^s \neq 0$, then the radial lobes are very pronounced. If, in contrast, $\mu_r^s \ll \sigma_r^s$, then the overlap between the two lobes increases and the radial velocity distribution is more box-like. We assume that the radial lobes, if present, are symmetric about $v_r = 0$ km/s, as this would be expected if the tidal debris originates from a satel-

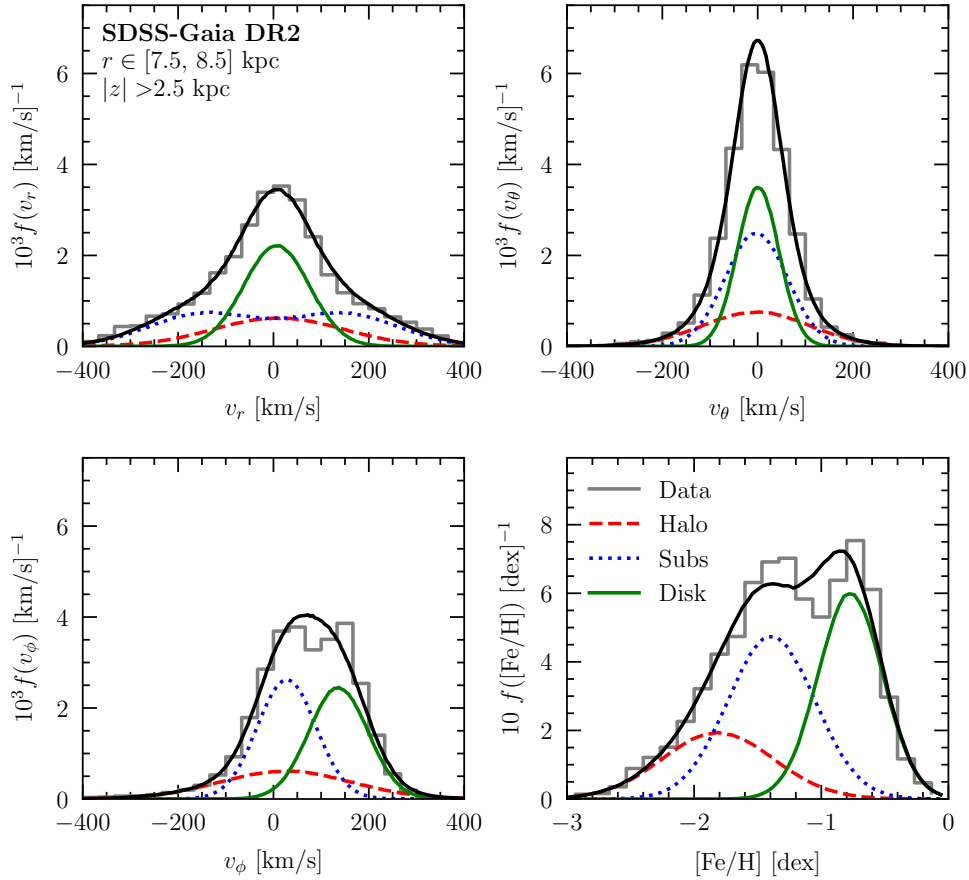


Figure 3. Posterior distributions of the spherical Galactocentric velocities and metallicity for the SDSS-*Gaia* DR2 sample in the region with $r \in [7.5, 8.5]$ kpc and $|z| > 2.5$ kpc (clockwise from top left: v_r , v_θ , $[Fe/H]$, and v_ϕ). In each panel, the disk, halo, and substructure distributions are shown as solid green, dashed red, and dotted blue lines, respectively. The data is represented by gray histograms.

lite as it moves towards ($v_r < 0$) and then away from ($v_r > 0$) the Galactic Center.⁴

The likelihood for the complete set of N stars is

$$p(\{O_i\} | \theta) = \prod_{i=1}^N \sum_{j=d,h,s} Q_j p_j(O_i | \theta), \quad (3)$$

where the brackets around the O_i indicate the full list of N values. Q_j is the probability that the star belongs to the j^{th} population; these represent two additional parameters in the model, as $Q_h = 1 - Q_d - Q_s$.

We use **emcee** (Foreman-Mackey et al. 2013) to find the posterior distributions of all 35 free parameters. In particular, we use 250 walkers, with 5000 steps, and a

burn-in period of 10000 steps. The priors for the separate parameters are provided in Table 1. We perform the mixture analysis in separate regions within the dashed aqua box of Fig. 1, which spans from $r \in [7.5, 10.0]$ kpc and $|z| > 2.5$ kpc. We find that the fit is well-behaved in this radial span, as gauged primarily by its ability to reproduce the expected properties of the baryonic disk. Below $|z| \sim 2.5$ kpc, we find a persistent systematic bias in the fitting procedure that results from modeling the azimuthal disk velocities as a single Gaussian (Schönrich & Binney 2012), so we do not present those results here.

3. THE STELLAR DISTRIBUTION

The 95% contours in metallicity–velocity space that are recovered from the analysis are overlaid on the separate panels of Fig. 2. These results apply specifically to the SDSS-*Gaia* DR2 sample in the region where $r \in [7.5, 8.5]$ kpc and $|z| > 2.5$ kpc. Clearly, the best-

⁴ For a visual example of the bimodal distribution, we point the reader to the top left panel of Fig. 6, which we will discuss in more detail in the following section.

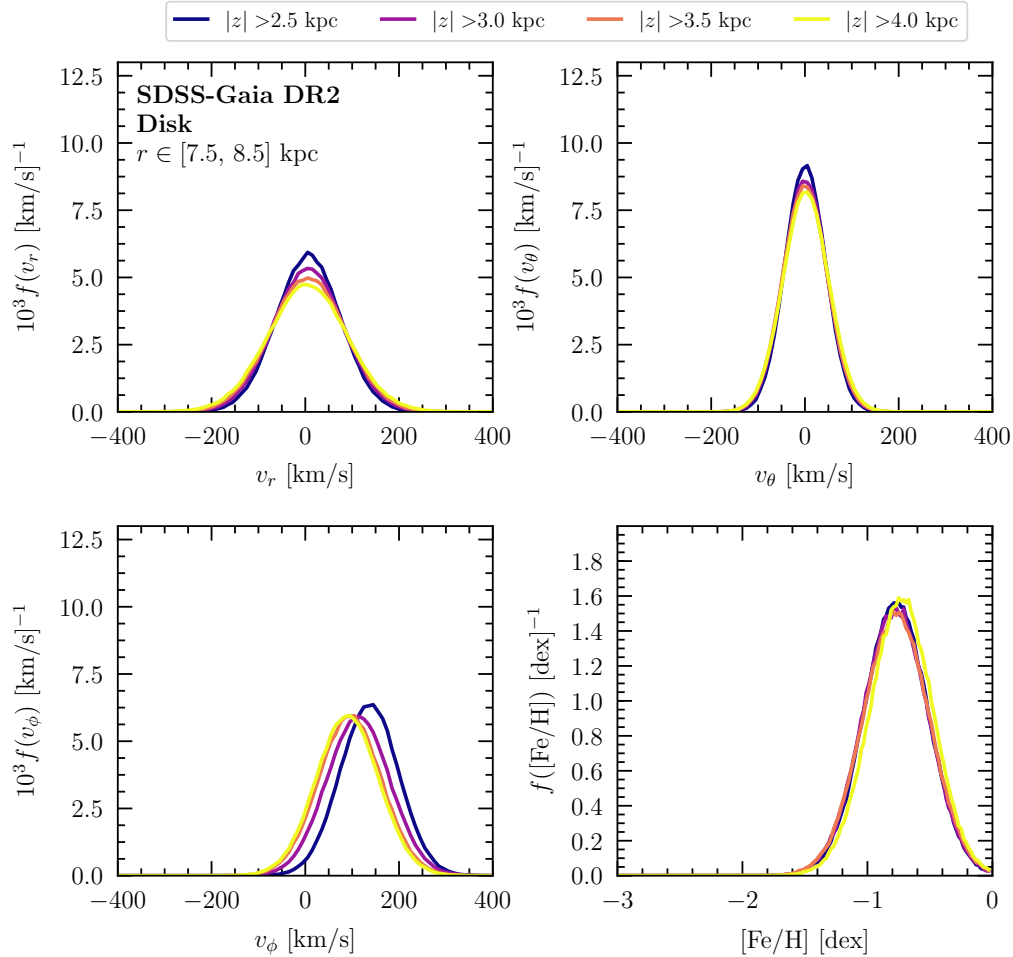


Figure 4. Posterior distributions for the disk population in the region with $r \in [7.5, 8.5]$ kpc (clockwise from top left: v_r , v_θ , $[\text{Fe}/\text{H}]$, and v_ϕ). We vary the distance from the mid-plane from $|z| > 2.5$ to 4.0 kpc.

fit distributions do an excellent job of picking out the population clusters that we identified by eye at the offset. Note that the priors are, for the most part, uninformative. They make no assumption about the relative metallicities of the halo and substructure populations, or the means and dispersions of their velocity distributions. The choice of priors gives the analysis enough freedom to explore both unimodal and bimodal distributions for the radial velocity of the substructure.

Fig. 3 shows the one-dimensional v_r , v_θ , v_ϕ , and $[\text{Fe}/\text{H}]$ posterior distributions for the same region. The disk, halo, and substructure distributions are indicated by the solid green, dashed red, and dotted blue lines, respectively, while the data is represented by the gray histograms. In the Appendix, we also provide the residuals between the model and data. One of the most surprising results is the degree to which the halo distribution is subdominant relative to the substructure. To better understand this, let us review in some detail the behavior of each population separately, and characterize its evolution as we vary the lower bound on $|z|$ in the range

from 2.5–4.0 kpc.

From Fig. 3, it is clear that the best-fit disk population recovers the peaks at $[\text{Fe}/\text{H}] = -0.77^5$ and $v_\phi = 136.3^{+1.9}_{-1.8}$ km/s that are observed in the data. Note that, in what follows, our convention is to quote the 16–50–84th percentiles. Fig. 4 demonstrates how the disk’s velocity and metallicity distribution vary away from the mid-plane. The $[\text{Fe}/\text{H}]$ and v_θ distributions remain essentially constant as one moves from $|z| > 2.5$ kpc to > 4 kpc. The v_r distribution broadens slightly and the median v_ϕ shifts to lower values, as expected from asymmetric drift (Bond et al. 2010)

Fig. 5 shows the corresponding distributions for the halo, which remain constant over the full z -range explored here. This population is clearly very metal-poor with a median $[\text{Fe}/\text{H}] = -1.82$. Its velocity distribution is nearly isotropic as $\sigma_r = 136.1^{+3.6}_{-3.6}$ km/s,

⁵ The errors on the best-fit metallicity means and dispersions quoted here are all on the order ± 0.01 dex.

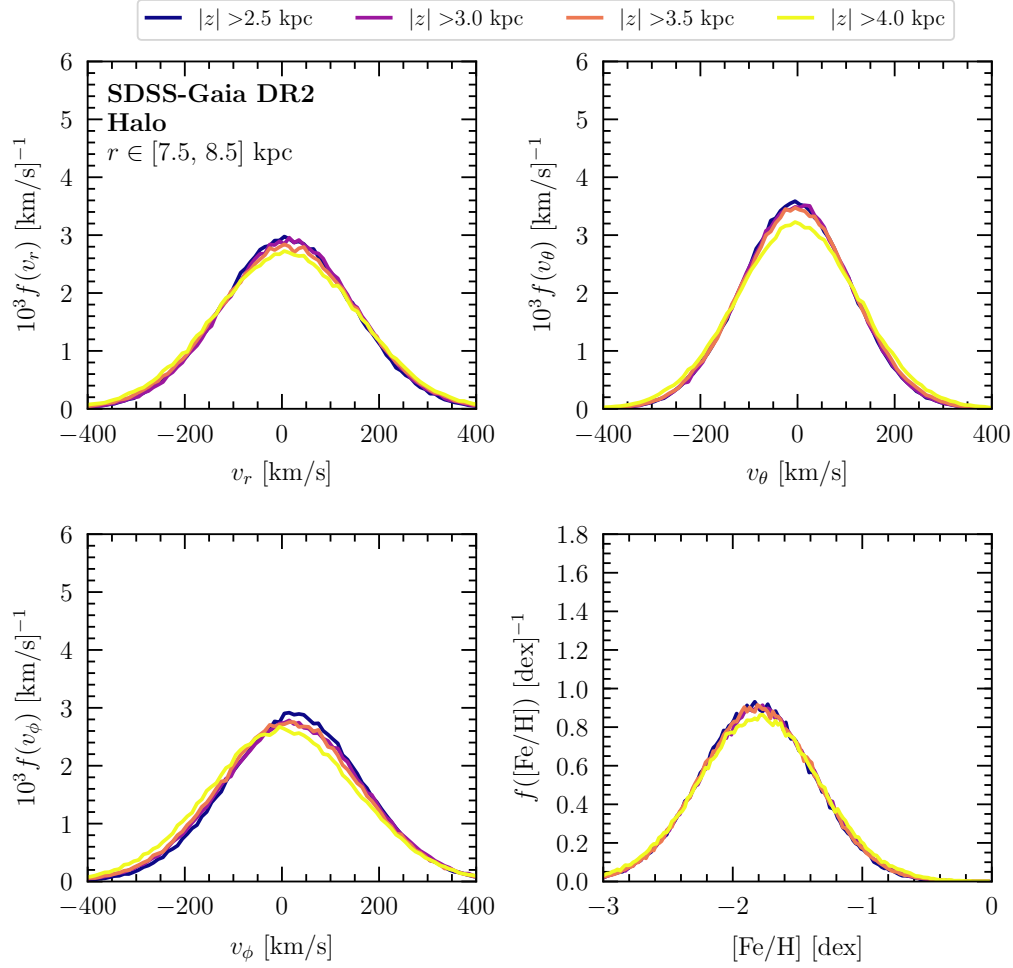


Figure 5. The same as Fig. 4, except for the halo population. The chemo-dynamic properties of the halo are invariant as one moves away from the Galactic mid-plane.

$\sigma_\theta = 112.5^{+4.1}_{-3.8}$ km/s, and $\sigma_\phi = 139.1^{+5.5}_{-5.2}$ km/s. The radial and azimuthal means are non-zero, with $\mu_r = 10.0^{+4.6}_{-4.9}$ km/s and $\mu_\phi = 24.9^{+5.6}_{-4.6}$ km/s. All three correlation coefficients are small: $(\rho_{r\theta}, \rho_{r\phi}, \rho_{\theta\phi}) = (-0.03^{+0.03}_{-0.03}, -0.08^{+0.03}_{-0.03}, 0.06^{+0.01}_{-0.02})$.

The halo is subdominant to the substructure, which is distinctive in both chemical abundance and kinematics. As shown in Fig. 6, the median metallicity of the substructure remains constant at $[\text{Fe}/\text{H}] = -1.39$ over all z -values. This population is more metal-rich, on average, than the halo, but more metal-poor than the disk. The radial velocity lobes are centered at $\mu_r = \pm 147.6^{+7.2}_{-6.4}$ km/s with $\sigma_r = 113.6^{+3.1}_{-3.0}$ km/s. There is no evidence for rotation in the polar direction ($\mu_\theta = -2.8^{+1.5}_{-1.6}$ km/s and $\sigma_\theta = 65.2^{+1.1}_{-1.2}$ km/s), however there is a larger offset in the azimuthal direction, with $\mu_\phi = 27.9^{+2.8}_{-2.9}$ km/s and $\sigma_\phi = 61.9^{+2.6}_{-2.9}$ km/s. The correlations $\rho_{r\theta}$ and $\rho_{\theta\phi}$ are consistent with zero, while $\rho_{r\phi} = 0.18^{+0.03}_{-0.03}$.

Fig. 7 shows the fractional contribution of the disk, halo, and substructure stars in the dataset. We see that

the disk contribution reduces from 40% at $|z| > 2.5$ kpc, down to 25% at $|z| > 4$ kpc. The halo contribution increases mildly in this range, as might be expected. However, the relative fraction of the substructure to the non-disk stellar population (right panel) is constant at $\sim 60\%$. We remind the reader that these fractional contributions pertain only to the dataset, and that metallicity biases can potentially affect the extrapolation to the Galaxy. However, the fact that the results are unchanged (within uncertainties) when the analysis is repeated on the subset of F/G stars, which exhibit minimal bias, gives us confidence in the results presented here.

We made the corresponding versions of Fig. 4–7 for $|z| > 2.5$ kpc and varying r in five equally sized bins from 7.5–10.0 kpc. These figures are provided in the Appendix. We observe no significant change in the velocity and metallicity distribution of the halo in this range. The substructure distributions are also stable, except that the radial lobes are further apart and more pronounced closer to the center of the Galaxy, as shown

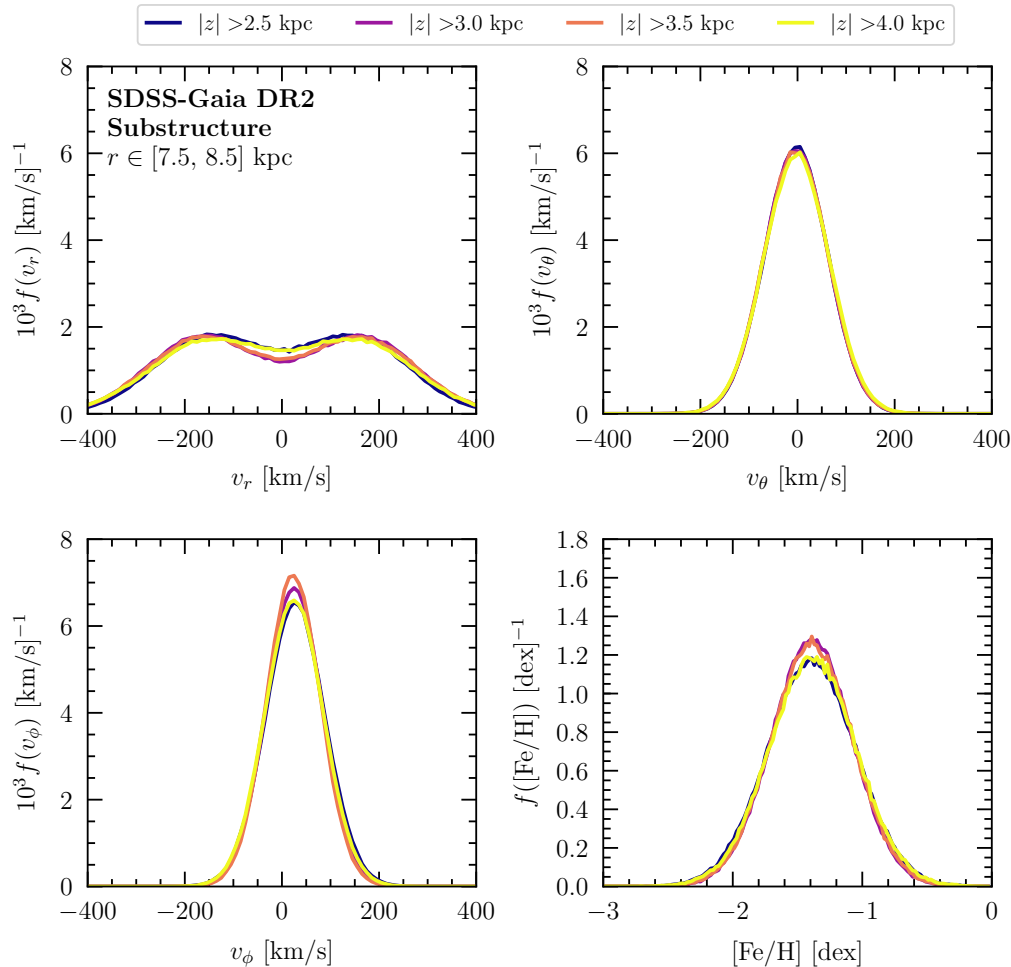


Figure 6. The same as Fig. 4, except for the substructure population. The radial distribution has characteristic lobes at ± 148 km/s that are likely related to tidal debris that is stripped as a merging satellite moves towards/away from the Galactic Center on its orbit. The distributions remain constant over the entire z -range.

in Fig. S4. The mean of the radial distribution is at $\mu_r = 140.5^{+8.4}_{-7.7}$ km/s with $\sigma_r = 114.5^{+4.1}_{-3.9}$ km/s for $r \in [7.5, 8.0]$ kpc, while it drops to $\mu_r = 115.0^{+3.1}_{-3.1}$ km/s with $\sigma_r = 104.2^{+2.7}_{-2.6}$ km/s for $r \in [9.5, 10]$ kpc. This may be related to features of the orbit that change with r .

The trends we observe are consistent with the interpretation that the substructure originates from the merger of a fairly massive satellite on a highly radial orbit (Belokurov et al. 2018a; Deason et al. 2018; Myeong et al. 2018). We distinguish two individual lobes in the radial velocity distribution, consistent with tidal debris that is preferentially stripped as the satellite moves towards/away from the Galactic Center. The small, but non-zero, azimuthal rotation may also be linked with the properties of the orbit. We note that our analysis cannot distinguish between one or more mergers. The latter situation seems unlikely as the metallicity of the substructure remains constant over the entire spatial range probed, which suggests a single progenitor. If multiple

mergers were at cause, the satellites would have to have similar masses and orbital properties, which seems fine-tuned.

It is challenging to directly compare our best-fit values to previous studies of the stellar halo, because we break down the sample into a Gaussian and non-Gaussian component at the likelihood level. As a result, the halo velocity distribution published in other works would be the weighted sum of our halo and substructure populations. However, the general trends we observe are roughly consistent with previous results. For example, previous studies found that halo stars with intermediate metallicities ($[\text{Fe}/\text{H}] \sim -1.4$) are radially anisotropic (Bond et al. 2010; Smith et al. 2009; Belokurov et al. 2018b), while stars on the more metal-poor end of the spectrum become more isotropic (Carollo et al. 2007, 2010; Herzog-Arbeitman et al. 2017b; Belokurov et al. 2018b).

4. THE DARK MATTER DISTRIBUTION

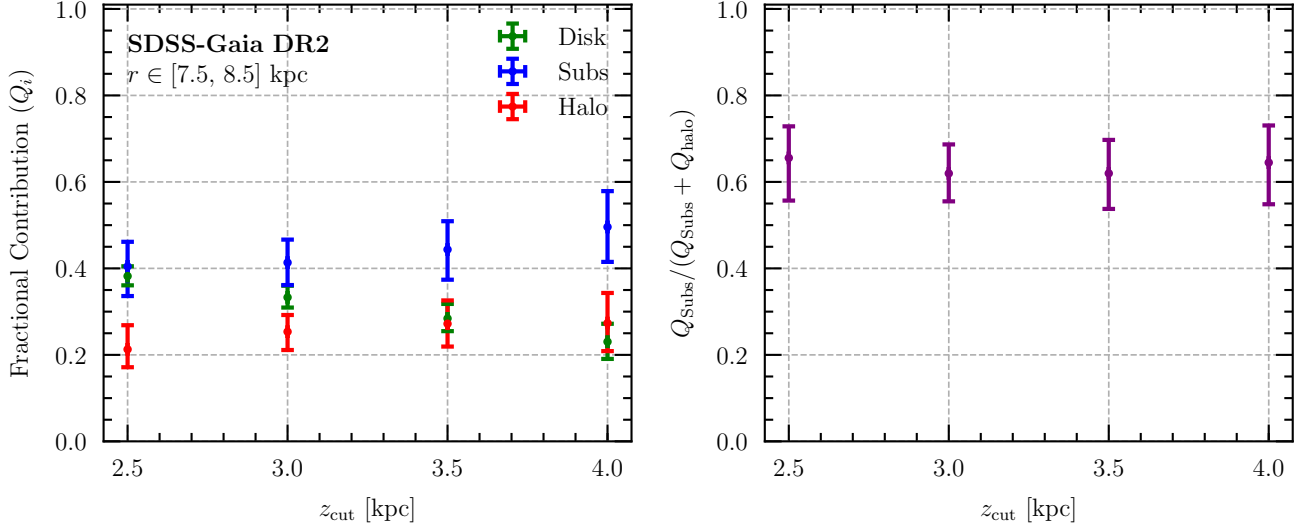


Figure 7. (Left) The fractional contribution of the disk (green), halo (red), and substructure (blue) populations in the dataset, for the region $r \in [7.5, 8.5]$ kpc and $|z| > z_{\text{cut}}$. The 2.1, 50, and 97.9th percentiles are shown here. (Right) The fraction of the substructure relative to all non-disk stars in the dataset.

4.1. Violating the Equilibrium Assumption

The distribution of DM velocities near the Solar position has important implications for the scattering rate in direct detection experiments (Goodman & Witten 1985). Drukier et al. (1986) were the first to recognize the importance of this contribution and hypothesized that the local DM velocities are well-modeled by a Maxwell-Boltzmann distribution, which has since become the standard in the field. We will begin by reviewing the arguments that motivate the Maxwell-

Boltzmann assumption and then demonstrate how they are challenged by the results of this study.

The observation of a flat rotation curve motivates a logarithmic potential for the Milky Way halo of the form $\Phi(r) = v_c^2 \ln(r) + \text{constant}$, where v_c is the circular velocity. If one assumes that the halo is in steady state and that its number density is described as a falling power law, $\nu \propto r^{-b}$, then there is a tight link between the value of the power-law index b , the potential Φ , and the phase-space distribution of the particles.

As an example, consider the radial Jeans equation, which is given by

$$\nu \frac{\partial \mu_r}{\partial t} + \nu \left(\mu_r \frac{\partial \mu_r}{\partial r} + \frac{\mu_\theta}{r} \frac{\partial \mu_r}{\partial \theta} + \frac{\mu_\phi}{r \sin \theta} \frac{\partial \mu_r}{\partial \phi} \right) + \frac{\partial (\nu \sigma_r^2)}{\partial r} + \frac{\nu}{r} [2\sigma_r^2 - (\sigma_\theta^2 + \sigma_\phi^2 + \mu_\theta^2 + \mu_\phi^2)] = -\nu \frac{\partial \Phi}{\partial r} \quad (4)$$

when the velocity components are uncorrelated. If all the DM is in an isotropic, equilibrated halo, then the time derivative in (4) vanishes, $\mu_r = \mu_\theta = \mu_\phi = 0$, and $\sigma_r = \sigma_\theta = \sigma_\phi$. In this limit, the Jeans equation simplifies to

$$\frac{\sigma_r^2}{\nu} \frac{\partial \nu}{\partial r} = -\frac{v_c^2}{r} \quad \longrightarrow \quad b = \frac{v_c^2}{\sigma_r^2}. \quad (5)$$

Taking the local circular velocity to be $v_c \sim 235$ km/s and a dispersion of $\sigma_r \sim 160$ km/s yields a power-law slope of $b \sim 2$. A density distribution of the form $\nu \sim r^{-2}$ is isothermal and one can use Poisson's equation to show that the associated velocity distribution is the Maxwell Boltzmann.

If the local DM is predominantly in substructure, then the derivation above fails because the DM is not in steady state nor is it necessarily isotropic. In this case, we must include all terms in (4). The time-dependent term may no longer be negligible and can cause particular challenges because it is difficult to quantify. We therefore lose predictive power in estimating the power-law density of the DM and inferring the corresponding velocity distribution through Poisson's equation.

The recourse we take is to rely on the fact that the DM shares a common origin with the accreted stellar population. N -body simulations have demonstrated that, for old enough mergers, the accreted stars are excel-

lent tracers of the underlying DM kinematics (Lisanti et al. 2015; Herzog-Arbeitman et al. 2017a). A subset of the authors are also completing a comprehensive study of the DM-stellar correlations using the FIRE hydrodynamic N -body simulations (Necib et al. 2018) that supports these general findings.

Therefore, we will assume that the accreted stellar population—that is, the halo and substructure—track the DM. In making this inference, we draw the startling conclusion that the majority of the local DM is in disequilibrium. Specifically, nearly all of the DM sourced from luminous satellites is in the class of kinematic substructure referred to as debris flow (Lisanti et al. 2015).

By assuming that the entire DM distribution traces the accreted stellar population, we ignore two other potential sources. The first is DM that accreted from small, dark subhalos. The second is DM that accreted diffusely, and thus does not originate in any bound structures that are tidally disrupted by the Milky Way. N -body simulations show that these DM contributions may be non-negligible near the Solar radius, depending on the merger history of the Galaxy (Wang et al. 2011). Just how large either of these contributions is in the Milky Way remains an open question; we plan to study their contribution in more detail in Necib et al. (2018).

4.2. Experimental Implications

In this section, we derive the heliocentric speed distribution for the halo and substructure populations, which we assume to trace the DM, and use it to calculate the scattering rate of a DM particle off a nuclear target. Ideally, we need the stellar velocity distribution at the Solar position, but this is also the region where the disk contribution dominates. Any mis-modeling of the disk may therefore strongly bias the fit results in this regime. For this reason, we restrict ourselves to $|z| > 2.5$ kpc. The results from Sec. 3 give us confidence that the halo and substructure distributions are likely invariant in z and that we can extrapolate them into the plane. Previous work (Belokurov et al. 2018b) also finds evidence for the radial substructure down to $|z| = 1$ kpc.

The posterior speed distribution in the heliocentric frame is shown in the left panel of Fig. 8, for heliocentric distance of $d_\odot < 4$ kpc and $|z| > 2.5$ kpc. To obtain this distribution, we draw values of v_r, v_θ , and v_ϕ from the full posterior distribution in the Galactic frame. Assuming that the stars are spatially uniform, we then transform to the heliocentric frame using the local rest-frame velocities $v_{\odot, \text{pec}} = (U, V, W) = (8.50, 13.38, 6.49)$ km/s (Coşkunoglu et al. 2011) and local circular velocity $v_c = 235$ km/s. The substructure and halo components are plotted separately (blue dotted and red dashed, respectively) and their total contribution is shown as the solid black line. Note how the relative

normalization of the substructure component strongly dominates at speeds $|v| \sim 250$ km/s.

For comparison, we also plot the Standard Halo Model (SHM) as the dashed gray line. The SHM is the speed distribution associated with the Maxwell Boltzmann (after integrating over the angular coordinates) and is defined as

$$f_{\text{SHM}}(v) = \frac{4v^2}{\sqrt{\pi}v_c^3} \exp\left[-\frac{v^2}{v_c^2}\right]. \quad (6)$$

The dispersion of the SHM is closest to that of the halo posterior, albeit slightly higher; the SHM is isotropic with $\sigma \sim 156$ km/s, while the best fits for the halo are $(\sigma_r, \sigma_\theta, \sigma_\phi) = (140.3^{+4.2}_{-4.9}, 114.2^{+3.3}_{-1.8}, 125.9^{+4.1}_{-3.4})$ km/s. The primary discrepancy with the SHM arises from the dominance of the substructure population. When this component is included, the total speed distribution is discrepant with the SHM. In this case, the polar and azimuthal velocities of the substructure are Gaussian with means $(\mu_\theta, \mu_\phi) = (-3.1^{+0.9}_{-0.9}, 35.5^{+1.8}_{-1.8})$ km/s and dispersions $(\sigma_\theta, \sigma_\phi) = (57.7^{+0.7}_{-0.8}, 61.2^{+1.5}_{-1.5})$ km/s, but the radial distribution has peaks at $\pm 117.7^{+1.8}_{-2.1}$ km/s, with a dispersion $\sigma_r = 108.2^{+1.2}_{-1.3}$ km/s for each. The substructure component arises from a more recent merger, as underlined by the fact that it is more metal-rich and highly radial. Because it is unvirialized, there is no reason why the SHM should model it well.

The empirical distribution clearly underestimates the fraction of high-speed DM particles, as compared to the SHM, which affects DM models where the minimum scattering speed, v_{\min} , needed to create a nuclear recoil of energy E_{nr} is high. For elastic scattering, the minimum speed depends both on the DM particle properties as well as the experiment as follows:

$$v_{\min} = \sqrt{\frac{m_N E_{\text{nr}}}{2\mu^2}}, \quad (7)$$

where m_N is the nuclear mass and μ is the DM-nucleus reduced mass. If the scattering is inelastic, then the minimum speed is even larger. The differential scattering rate, per unit detector mass, for the most common operators is then

$$\frac{dR}{dE_{\text{nr}}} = \frac{\rho_\chi}{2m_\chi \mu^2} \sigma(q) g(v_{\min}), \quad (8)$$

where m_χ is the DM particle mass and ρ_χ its local density, $\sigma(q)$ is an effective scattering cross section that depends on the momentum transfer q , and the mean inverse speed is defined as

$$g(v_{\min}) = \int_{v_{\min}}^{\infty} \frac{\tilde{f}(v)}{v} dv, \quad (9)$$

where $\tilde{f}(v)$ is the heliocentric velocity distribution.

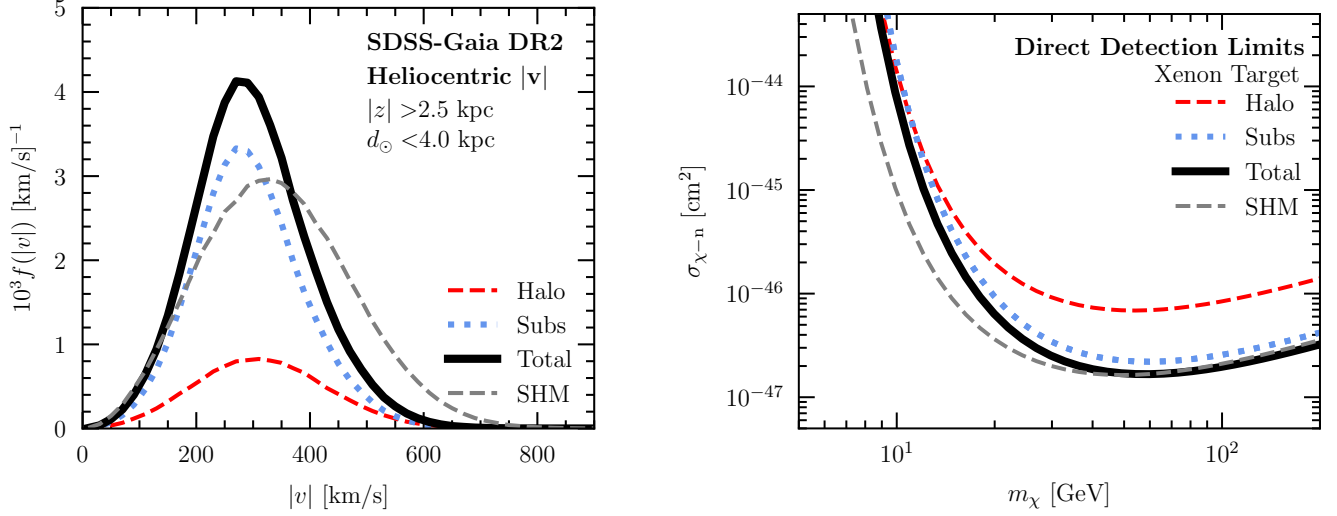


Figure 8. (Left) Posterior speed distribution for the halo (dashed red) and substructure (dotted blue) components. The solid black line represents the total contribution. These results are based on fits to the SDSS-*Gaia* DR2 data within heliocentric distances of $d_\odot < 4$ kpc and $|z| > 2.5$ kpc. For comparison, we show the Standard Halo Model (dashed gray), defined in (6). The empirical distribution does not include contributions from DM accreted from non-luminous satellites or diffusely. (Right) The 95% background-free C.L. limits on the DM-nucleon scattering cross section, $\sigma_{\chi-n}$, for spin-independent interactions as a function of DM mass, m_χ , assuming a xenon target with an exposure of 1 kton \times year exposure and a 4.9 keV_{nr} energy threshold. These limits are illustrative and do not account for experimental energy efficiencies near threshold (Aprile et al. 2018).

The right panel of Fig. 8 shows the corresponding limits on the DM mass and DM-nucleon scattering cross section, $\sigma_{\chi-n}$, assuming the simplest spin-independent operator. For this example, we assume a xenon target, energy threshold of 4.9 keV_{nr}, and exposure of 1 kton \times year. The 95% one-sided Poisson C.L. limit (3 events) obtained using the velocity distribution inferred from SDSS-*Gaia* DR2 is shown in solid black, and compared to the SHM in dashed grey. The substructure component drives the sensitivity at all masses, while the halo contribution is subdominant, but becomes more important at lower masses. In both cases, the exclusion is significantly weakened for $m_\chi \lesssim 30$ GeV relative to that obtained using the SHM. For $m_\chi \gtrsim 100$ GeV, the black and gray-dashed lines approach each other because $v_{\min} \rightarrow 0$ in (9).

The overall effect of the empirical velocity distribution on the scattering limit depends on the details of the nuclear target, experimental threshold, and DM mass—all parameters that feed into the minimum scattering speed defined in (7). A more model- and experiment-independent way of understanding these effects is to study the dependence of the time-averaged inverse-speed, $\langle g(v_{\min}) \rangle$, as a function of the minimum speed, as this term captures the dependence of the scattering rate on the DM velocities. The left panel of Fig. 9 plots this quantity for the empirical speed distribution obtained in this work (solid black) and the SHM (dashed gray). The scattering rate for the empirical distribution is reduced relative to that for the SHM at $v_{\min} \gtrsim 300$ km/s;

it is enhanced for lower minimum speeds. The scattering rate is completely suppressed for $v_{\min} \gtrsim 550$ km/s, whereas the SHM continues to contribute events above this point.

To better understand the implications of these results, let us consider the concrete example of a 10 GeV DM particle interacting in several detectors. Such a DM particle needs a minimum speed of ~ 570 km/s to scatter a xenon nucleus at an energy of ~ 5 keV_{nr} in Xenon1T (Aprile et al. 2018). As seen from the left panel of Fig. 9, this is highly suppressed relative to the SHM expectation.⁶ In contrast, the DarkSide-50 low-mass analysis (Agnes et al. 2018) can detect argon recoils down to 0.6 keV_{nr} in energy. A 10 GeV DM particle only needs speeds of ~ 130 km/s to create such a recoil and these speeds are well-supported by the empirical distribution.

The empirical velocity distribution also impacts the time-dependence of a signal. The DM scattering rate should modulate annually due to the Earth’s motion around the Sun (Drukier et al. 1986).

The right panel of Fig. 9 compares the modulation amplitude assuming the newly derived velocity distribution, as compared to the SHM. To obtain the amplitude, we transform the velocities from the Galactic to the heliocentric frame, taking into account the Earth’s time-dependent velocity as defined in Lee et al. (2013).

⁶ In actuality, Xenon1T has non-zero efficiency below ~ 5 keV_{nr}, which improves its sensitivity in this range.

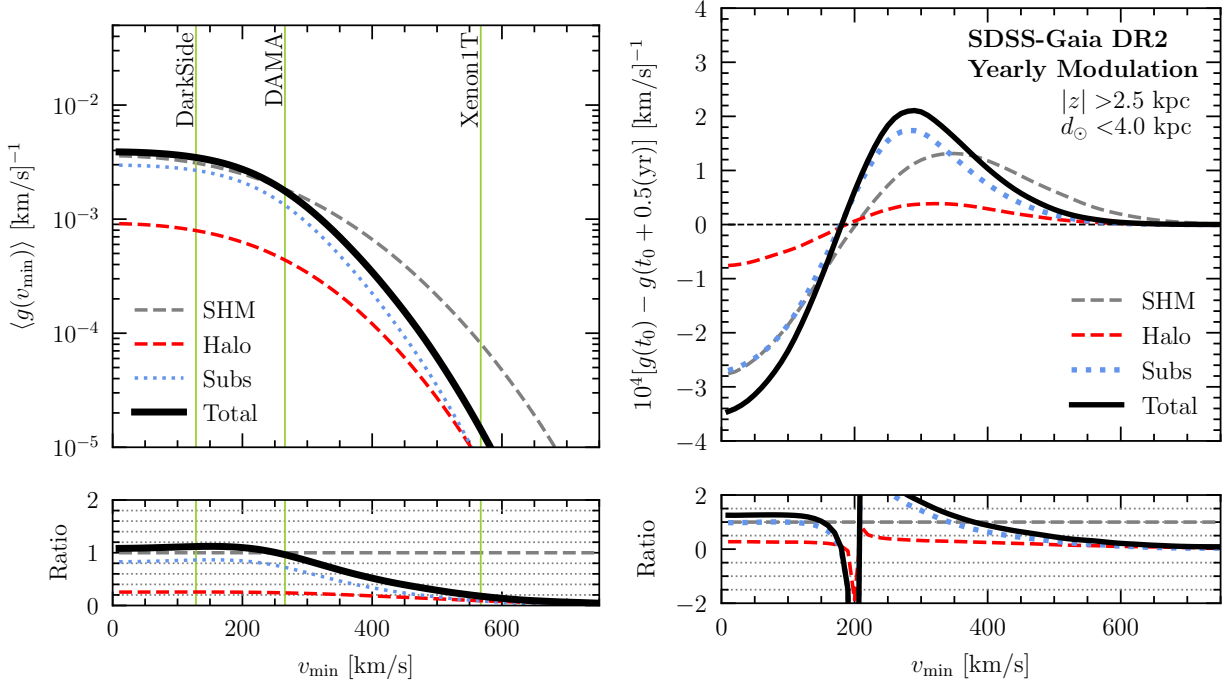


Figure 9. (Left) Time-averaged inverse speed distribution defined in (9) as a function of the minimum scattering speed, v_{\min} . The substructure and halo distributions are shown as the dotted blue and dashed red lines, respectively, and their total contribution is shown as solid black. The SHM expectation is the dashed gray line. The vertical green lines indicate the values of v_{\min} near threshold for a 10 GeV dark matter particle scattering in the DarkSide-50 (Agnes et al. 2018), DAMA (Bernabei et al. 2018), and Xenon1T (Aprile et al. 2018) detectors. (Right) Expected yearly modulation amplitude between June ($t_0 \approx 150$ days) and December as a function of v_{\min} .

We do not include the effect of gravitational focusing, which may further affect the properties of the modulation signal (Lee et al. 2014).

The modulation amplitude for the SHM exhibits the expected features: a maximum when $v_{\min} \sim 350$ km/s and a change in phase below ~ 200 km/s—see Freese et al. (2013) for a review. In comparison, the modulation amplitude obtained from the SDSS-*Gaia* DR2 distribution is maximal closer to $v_{\min} \sim 250$ km/s and falls off faster towards higher v_{\min} . This is due to the fact that the empirical velocity distribution $f(v)$ is less broad than the SHM. Therefore, the differences in the heliocentric speed distribution over the year are typically more pronounced, but over a smaller range of v_{\min} . The DAMA experiment, which claims an annually modulating signal, has a NaI target and threshold energy of ~ 3.3 keV_{nr} (Bernabei et al. 2018). An observable scatter of a 10 GeV DM particle off a Na nucleus requires a minimum speed of ~ 270 km/s. We note that this falls in the region where the empirical distribution has a significant effect on the modulation amplitude, and motivates a more careful study of the consistency with data.

The results shown here are specific to spin-independent interactions. However, the new velocity distribution will have an effect on other interaction

operators—as the dependence of some of these operators on the DM momentum is non-trivial, the magnitude of the effects can vary from operator to operator (Fan et al. 2010; Fitzpatrick et al. 2013, 2012; Lisanti 2017). Similarly, the velocity distribution will also be relevant for the interpretation of DM-electron scattering interactions—see Battaglieri et al. (2017) for a review—and axion experiments (Ling et al. 2004; Hoskins et al. 2016; Sloan et al. 2016; Vergados & Semertzidis 2017; Millar et al. 2017; Foster et al. 2017).

5. CONCLUSIONS

We performed a mixture model analysis on Main Sequence stars in the SDSS-*Gaia* DR2 catalog within the range $r \in [7.5, 10.0]$ kpc and $|z| > 2.5$ kpc. The full chemo-dynamic properties of the stars (\mathbf{v} , $[\text{Fe}/\text{H}]$) were used to identify the populations most likely belonging to the disk and halo, as well as any potential kinematic substructure. The velocities of the disk and halo stars were modeled as multivariate normal distributions, while the substructure component was given the freedom to scan non-Gaussian possibilities.

The recovered disk, halo, and substructure populations have median metallicities of $[\text{Fe}/\text{H}] = -0.8, -1.8$, and -1.4 respectively. The disk component acts as expected within the region studied here. The halo compo-

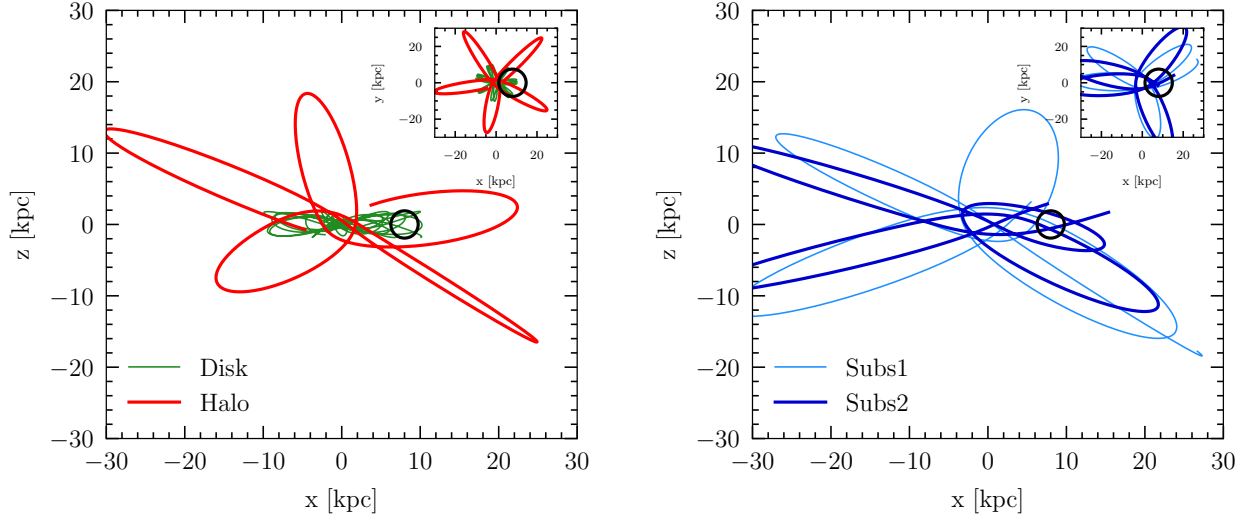


Figure 10. (Left) Orbits of stars that likely belong to the disk (green) and halo (red) populations. (Right) The corresponding orbits for two likely substructure stars, labeled as ‘Subs1’ and ‘Subs2.’ The main figure shows the projection in the $x - z$ plane, while the inset shows that of the $x - y$ plane. The black circle shows the location of the Sun.

ment is very metal-poor and its velocity ellipsoid is nearly isotropic. The analysis identifies a substructure population of intermediate metallicity stars whose radial velocities are best modeled with a non-Gaussian distribution. This population had been identified in previous work as the *Gaia* Sausage (Belokurov et al. 2018b). Our analysis provides the first model for its velocity and metallicity distribution, and clearly distinguishes its contribution relative to the disk and metal-poor halo over the full metallicity range of the sample.

The substructure population is anisotropic in velocity, with two broad lobes centered at $v_r \sim \pm 150$ km/s. It can be explained as tidal debris from a satellite galaxy on a highly radial orbit. The lobes are consistent with debris that is torn off as the satellite moves towards/away from the Galactic Center while orbiting. The distinctive metallicity of the substructure strongly suggests that it is sourced by a single progenitor.

To illustrate these points, Fig. 10 compares the orbits of a likely halo, disk, and substructure star, chosen at random—see also Deason et al. (2018). We use the *gala* package (Price-Whelan et al. 2017) to integrate the orbits back 1 Myr, given the star’s present-day position and velocity, and assume the default Milky Way potential from Bovy (2015). In the left panel, we plot the orbit of a likely disk (green line) and halo (red line) star. The disk star is confined to the plane, as expected, while the halo star’s orbit is more isotropic. We contrast this to the orbits of two likely substructure stars in the right panel, indicated by the dark and light blue lines. The orbits of these stars are highly radial and have a lower inclination angle relative to the mid-plane.

As the substructure is fairly hot and exhibits no ob-

vious spatial features in the local region studied here, it likely originated from an old merger. Using the stellar-mass metallicity relation of Kirby et al. (2013) and the median metallicity of the substructure component, we estimate that its progenitor had stellar mass $M_* \sim 10^{7-8} M_\odot$. We note that the Sagittarius dwarf galaxy (Ibata et al. 1994) cannot be the progenitor of the substructure as it is a younger merger event and its orbit is less eccentric (Law & Majewski 2010; Purcell et al. 2011). In particular, the apocenter to pericenter ratio of Sagittarius is 5:1, whereas it is 20:1 for the substructure.

Our study of the local stellar distribution has direct relevance for DM. N -body simulations have demonstrated that the old metal-poor halo is a good tracer of the virialized DM kinematics. Additionally, kinematic substructure such as DM debris flow have been shown to have stellar counterparts. If the accreted stellar component in the SDSS-*Gaia* DR2 sample (*e.g.*, the halo and substructure populations) are adequate DM tracers, then our results imply that a significant fraction of the local DM is in debris flow.

We find that the halo and substructure populations do not depend on the vertical distance off the plane, at least in the region from $|z| > 2.5$ –4 kpc. This gives us confidence in extrapolating their contributions to the Solar neighborhood, which is relevant for direct detection experiments. By performing a more detailed modeling of the disk component, one could potentially extend the mixture analysis to lower z and recover the accreted stellar distribution directly in this region. We plan to pursue this in future work.

The heliocentric speed distribution that we derive

from SDSS-*Gaia* DR2 within heliocentric distances $d_{\odot} < 4$ kpc and $|z| > 2.5$ kpc is incompatible with the SHM. The inferred DM distribution has far fewer high-speed particles than expected from the SHM. The fact that the DM is generally slower reduces the sensitivity to DM that is not energetic enough to create observable nuclear recoils in a detector target. We have demonstrated that the limits of an experiment using a xenon target are suppressed below $m_{\text{DM}} \lesssim 30$ GeV for the case of spin-independent interactions. The overall size of the suppression can vary for different nuclear target masses, as well as different scattering operators. Current exclusion limits and future projections should be revisited in light of these new findings.

The SDSS-*Gaia* DR2 study provides the first indication that the local DM is in disequilibrium. Given these results, it is pressing to better quantify just how well the stars and DM track each other in simulated mergers that resemble the observations. Additionally, we need to quantify the effects of DM that is diffuse or originates from non-luminous subhalos. If either of these dominates locally, then the total DM distribution will differ from that accreted by the largest satellites. In a follow-up study, a subset of the authors will begin to address these points using the FIRE simulations (Necib et al. 2018).

ACKNOWLEDGEMENTS

We would like to thank J. Bochanski, J. Bovy, G. Collin, A. Drlica-Wagner, D. Hogg, K. Hawkins, L. Lancaster, T. Li, S. McDermott, D. Spergel, and N. Weiner for useful conversations. We also acknowledge use of the *Astropy* (Astropy Collaboration et al. 2013), *emcee* (Foreman-Mackey et al. 2013), *gala* (Price-Whelan et al. 2017), and *IPython* (Pérez & Granger 2007) software packages. This project was developed in part at the NYC *Gaia* DR2 Workshop in 2018 April, as well as the 2018 NYC *Gaia* Sprint, hosted by the Center for Computational Astrophysics of the Flatiron Institute in New York City.

LN is supported by the DOE under Award Number DESC0011632, and the Sherman Fairchild fellowship. ML is supported by the DOE under Award Number DESC0007968, the Alfred P. Sloan Foundation and the Cottrell Scholar Program through the Research Corporation for Science Advancement. VB is supported by the European Research Council under the European Union’s Seventh Framework Programme (FP/2007-2013) / ERC Grant Agreement n. 308024. This paper made use of the Whole Sky Database (WSDb) created by Sergey Koposov and maintained at the Institute of Astronomy, Cambridge by Sergey Koposov, Vasily Belokurov and Wyn Evans with financial support from the Science & Technology Facilities Council (STFC) and the European

Research Council (ERC).

This work has made use of data from the European Space Agency (ESA) mission *Gaia* (<https://www.cosmos.esa.int/gaia>), processed by the *Gaia* Data Processing and Analysis Consortium (DPAC, <https://www.cosmos.esa.int/web/gaia/dpac/consortium>). Funding for the DPAC has been provided by national institutions, in particular the institutions participating in the *Gaia* Multilateral Agreement.

Funding for SDSS-III has been provided by the Alfred P. Sloan Foundation, the Participating Institutions, the National Science Foundation, and the U.S. Department of Energy Office of Science. The SDSS-III web site is <http://www.sdss3.org/>.

SDSS-III is managed by the Astrophysical Research Consortium for the Participating Institutions of the SDSS-III Collaboration including the University of Arizona, the Brazilian Participation Group, Brookhaven National Laboratory, Carnegie Mellon University, University of Florida, the French Participation Group, the German Participation Group, Harvard University, the Instituto de Astrofísica de Canarias, the Michigan State/Notre Dame/JINA Participation Group, Johns Hopkins University, Lawrence Berkeley National Laboratory, Max Planck Institute for Astrophysics, Max Planck Institute for Extraterrestrial Physics, New Mexico State University, New York University, Ohio State University, Pennsylvania State University, University of Portsmouth, Princeton University, the Spanish Participation Group, University of Tokyo, University of Utah, Vanderbilt University, University of Virginia, University of Washington, and Yale University.

REFERENCES

- Agnes, P., et al. 2018, arXiv:1802.06994
- Ahn, C. P., Alexandroff, R., Allende Prieto, C., et al. 2012, *ApJS*, 203, 21
- Aprile, E., et al. 2018, arXiv:1805.12562
- Astropy Collaboration, Robitaille, T. P., Tollerud, E. J., et al. 2013, *AAP*, 558, A33
- Bahcall, J. N., & Soneira, R. M. 1980, *ApJS*, 44, 73
- Battaglieri, M., et al. 2017, arXiv:1707.04591
- Belokurov, V., Deason, A. J., Koposov, S. E., et al. 2018a, *MNRAS*, 477, 1472
- Belokurov, V., Erkal, D., Evans, N. W., Koposov, S. E., & Deason, A. J. 2018b, *MNRAS*, 478, 611
- Bernabei, R., et al. 2018, arXiv:1805.10486
- Bhattacharjee, P., Chaudhury, S., Kundu, S., & Majumdar, S. 2013, *Phys. Rev.*, D87, 083525
- Blitz, L. 1979, *ApJL*, 231, L115
- Bond, N. A., et al. 2010, *Astrophys. J.*, 716, 1
- Bovy, J. 2015, *The Astrophysical Journal Supplement Series*, 216, 29
- Bozorgnia, N., & Bertone, G. 2017, arXiv:1705.05853
- Bozorgnia, N., Catena, R., & Schwetz, T. 2013, *JCAP*, 12, 050
- Bozorgnia, N., et al. 2016, *JCAP*, 1605, 024
- Burton, W. B., & Gordon, M. A. 1978, *A&A*, 63, 7
- Caldwell, J. A. R., & Ostriker, J. P. 1981, *Astrophys. J.*, 251, 61
- Carollo, D., et al. 2007, *Nature*, 450, 1020
- Carollo, D., Beers, T. C., Chiba, M., et al. 2010, *Astrophys. J.*, 712, 692
- Catena, R., & Ullio, P. 2012, *JCAP*, 5, 005
- Chaudhury, S., Bhattacharjee, P., & Cowsik, R. 2010, *JCAP*, 1009, 020
- Clemens, D. P. 1985, *ApJ*, 295, 422
- Coşkunoglu, B., Ak, S., Bilir, S., et al. 2011, *MNRAS*, 412, 1237
- Cooper, A. P., Cole, S., Frenk, C. S., et al. 2010, *MNRAS*, 406, 744
- Deason, A. J., Belokurov, V., Evans, N. W., & Johnston, K. V. 2013, *Astrophys. J.*, 763, 113
- Deason, A. J., Belokurov, V., Koposov, S. E., & Lancaster, L. 2018, *ArXiv e-prints*, arXiv:1805.10288
- Deason, A. J., Belokurov, V., & Weisz, D. R. 2015, *MNRAS*, 448, L77
- Del Nobile, E. 2014, *Adv. High Energy Phys.*, 2014, 604914
- Diemand, J., Kuhlen, M., & Madau, P. 2007, *Astrophys. J.*, 667, 859
- Diemand, J., Kuhlen, M., Madau, P., et al. 2008, *Nature*, 454, 735
- Drukier, A. K., Freese, K., & Spergel, D. N. 1986, *Phys. Rev.*, D33, 3495
- Elahi, P. J., Thacker, R. J., & Widrow, L. M. 2011, *Mon. Not. Roy. Astron. Soc.*, 418, 320
- ESA, ed. 1997, *ESA Special Publication*, Vol. 1200, *The HIPPARCOS and TYCHO catalogues. Astrometric and photometric star catalogues derived from the ESA HIPPARCOS Space Astrometry Mission*
- Fairbairn, M., & Schwetz, T. 2009, *JCAP*, 0901, 037
- Fan, J., Reece, M., & Wang, L.-T. 2010, *JCAP*, 1011, 042
- Fich, M., Blitz, L., & Stark, A. A. 1989, *ApJ*, 342, 272
- Fiorentino, G., Bono, G., Monelli, M., et al. 2015, *ApJ*, 798, L12
- Fitzpatrick, A. L., Haxton, W., Katz, E., Lubbers, N., & Xu, Y. 2012, arXiv:1211.2818
- . 2013, *JCAP*, 1302, 004
- Foreman-Mackey, D., Hogg, D. W., Lang, D., & Goodman, J. 2013, *PASP*, 125, 306
- Fornasa, M., & Green, A. M. 2014, *Phys. Rev.*, D89, 063531
- Foster, J. W., Rodd, N. L., & Safdi, B. R. 2017, arXiv:1711.10489
- Freese, K., Frieman, J. A., & Gould, A. 1988, *Phys. Rev.*, D37, 3388
- Freese, K., Lisanti, M., & Savage, C. 2013, *Rev. Mod. Phys.*, 85, 1561
- Gaia Collaboration, Brown, A. G. A., Vallenari, A., et al. 2018, *ArXiv e-prints*, arXiv:1804.09365
- Gaia Collaboration, Prusti, T., de Bruijne, J. H. J., et al. 2016, *A&A*, 595, A1
- Goodman, M. W., & Witten, E. 1985, *Phys. Rev.*, D31, 3059
- Green, A. M. 2017, *J. Phys.*, G44, 084001
- Hansen, S. H., & Moore, B. 2006, *New Astron.*, 11, 333
- Helmi, A. 2008, *A&A Rv*, 15, 145
- Helmi, A., Babusiaux, C., Koppelman, H. H., et al. 2018, *ArXiv e-prints*, arXiv:1806.06038
- Helmi, A., & White, S. D. M. 1999, *Mon. Not. Roy. Astron. Soc.*, 307, 495
- Herzog-Arbeitman, J., Lisanti, M., Madau, P., & Necib, L. 2017a, arXiv:1704.04499
- Herzog-Arbeitman, J., Lisanti, M., & Necib, L. 2017b, arXiv:1708.03635
- Hoskins, J., et al. 2016, *Phys. Rev.*, D94, 082001
- Ibata, R. A., Gilmore, G., & Irwin, M. J. 1994, *Nature*, 370, 194
- Ivezic, Z., et al. 2008, *Astrophys. J.*, 684, 287
- Jeans, J. H. 1922, *MNRAS*, 82, 122
- Johnston, K. V., Bullock, J. S., Sharma, S., et al. 2008, *Astrophys. J.*, 689, 936
- Jungman, G., Kamionkowski, M., & Griest, K. 1996, *PhR*, 267, 195
- Kapteyn, J. C. 1922, *ApJ*, 55, 302
- Kelso, C., et al. 2016, *JCAP*, 1608, 071
- Kirby, E. N., Cohen, J. G., Guhathakurta, P., et al. 2013, *Astrophys. J.*, 779, 102
- Knapp, G. R., Stark, A. A., & Wilson, R. W. 1985, *AJ*, 90, 254
- Koposov, S., & Bartunov, O. 2006, in *Astronomical Society of the Pacific Conference Series*, Vol. 351, *Astronomical Data Analysis Software and Systems XV*, ed. C. Gabriel, C. Arviset, D. Ponz, & S. Enrique, 735
- Kuhlen, M., Lisanti, M., & Spergel, D. N. 2012, *Phys. Rev.*, D86, 063505
- Kuhlen, M., Weiner, N., Diemand, J., et al. 2010, *JCAP*, 1002, 030
- Kunder, A., Kordopatis, G., Steinmetz, M., et al. 2017, *AJ*, 153, 75
- Lancaster, L., Koposov, S., Belokurov, V., Evans, N. W., & Deason, A. 2018
- Law, D. R., & Majewski, S. R. 2010, *Astrophys. J.*, 714, 229
- Lee, S. K., Lisanti, M., Peter, A. H. G., & Safdi, B. R. 2014, *Phys. Rev. Lett.*, 112, 011301
- Lee, S. K., Lisanti, M., & Safdi, B. R. 2013, *JCAP*, 1311, 033
- Ling, F. S., Nezri, E., Athanassoula, E., & Teyssier, R. 2010, *JCAP*, 1002, 012
- Ling, F.-S., Sikivie, P., & Wick, S. 2004, *Phys. Rev.*, D70, 123503
- Lisanti, M. 2017, in *Proceedings, Theoretical Advanced Study Institute in Elementary Particle Physics: New Frontiers in Fields and Strings (TASI 2015)*: Boulder, CO, USA, June 1-26, 2015, 399–446
- Lisanti, M., & Spergel, D. N. 2012, *Phys. Dark Univ.*, 1, 155
- Lisanti, M., Spergel, D. N., & Madau, P. 2015, *Astrophys. J.*, 807, 14
- Lisanti, M., Strigari, L. E., Wacker, J. G., & Wechsler, R. H. 2011, *Phys. Rev.*, D83, 023519
- Maciejewski, M., Vogelsberger, M., White, S. D. M., & Springel, V. 2011, *Mon. Not. Roy. Astron. Soc.*, 415, 2475
- Mandal, S., Majumdar, S., Rentala, V., & Basu Thakur, R. 2018, arXiv:1806.06872

- Mao, Y.-Y., Strigari, L. E., Wechsler, R. H., Wu, H.-Y., & Hahn, O. 2013, *Astrophys. J.*, 764, 35
- March-Russell, J., McCabe, C., & McCullough, M. 2009, *JHEP*, 05, 071
- Millar, A. J., Redondo, J., & Steffen, F. D. 2017, *JCAP*, 1710, 006
- Myeong, G. C., Evans, N. W., Belokurov, V., Sanders, J. L., & Koposov, S. E. 2018, [arXiv:1805.00453](https://arxiv.org/abs/1805.00453)
- Necib, L., Lisanti, M., Garisson-Kimmel, S., et al. 2018, In preparation
- Oort, J. H. 1932, *BAN*, 6, 249
- Ostriker, J. P., Peebles, P. J. E., & Yahil, A. 1974, *ApJL*, 193, L1
- Pérez, F., & Granger, B. E. 2007, *Computing in Science and Engineering*, 9, 21
- Pillepich, A., Kuhlen, M., Guedes, J., & Madau, P. 2014, *ApJ*, 784, 161
- Pont, F., Mayor, M., & Burki, G. 1994, *A&A*, 285, 415
- Price-Whelan, A., Sipocz, B., Major, S., & Oh, S. 2017, [adrm/gala, v.0.2.1, Zenodo, doi:10.5281/zenodo.833339](https://doi.org/10.5281/zenodo.833339)
- Purcell, C. W., Bullock, J. S., Tollerud, E., Rocha, M., & Chakrabarti, S. 2011, *Nature*, 477, 301
- Read, J. I. 2014, *J. Phys.*, G41, 063101
- Schlegel, D. J., Finkbeiner, D. P., & Davis, M. 1998, *Astrophys. J.*, 500, 525
- Schönrich, R. 2012, *Monthly Notices of the Royal Astronomical Society*, 427, 274
- Schönrich, R., & Binney, J. 2012, *MNRAS*, 419, 1546
- Sloan, J. V., et al. 2016, *Phys. Dark Univ.*, 14, 95
- Sloane, J. D., Buckley, M. R., Brooks, A. M., & Governato, F. 2016, [arXiv:1601.05402](https://arxiv.org/abs/1601.05402)
- Smith, M. C., Evans, N. W., Belokurov, V., et al. 2009, *Mon. Not. Roy. Astron. Soc.*, 399, 1223
- Venn, K. A., Irwin, M., Shetrone, M. D., et al. 2004, *AJ*, 128, 1177
- Vergados, J. D., & Semertzidis, Y. K. 2017, *Nuclear Physics B*, 915, 10
- Vogelsberger, M., & White, S. D. M. 2011, *MNRAS*, 413, 1419
- Vogelsberger, M., Helmi, A., Springel, V., et al. 2009, *Mon. Not. Roy. Astron. Soc.*, 395, 797
- Wang, J., Navarro, J. F., Frenk, C. S., et al. 2011, *MNRAS*, 413, 1373
- White, S. D. M., & Rees, M. J. 1978, *Mon. Not. Roy. Astron. Soc.*, 183, 341
- Yanny, B., et al. 2009, *Astron. J.*, 137, 4377
- Zemp, M., Diemand, J., Kuhlen, M., et al. 2009, *Mon. Not. Roy. Astron. Soc.*, 394, 641

APPENDIX

In this Appendix, we include some additional figures to supplement the discussion in the main text. We provide residual maps that demonstrate the quality of the model fit, and show how the results in the main text vary in five radial bins from $r = 7.5$ to 10 kpc.

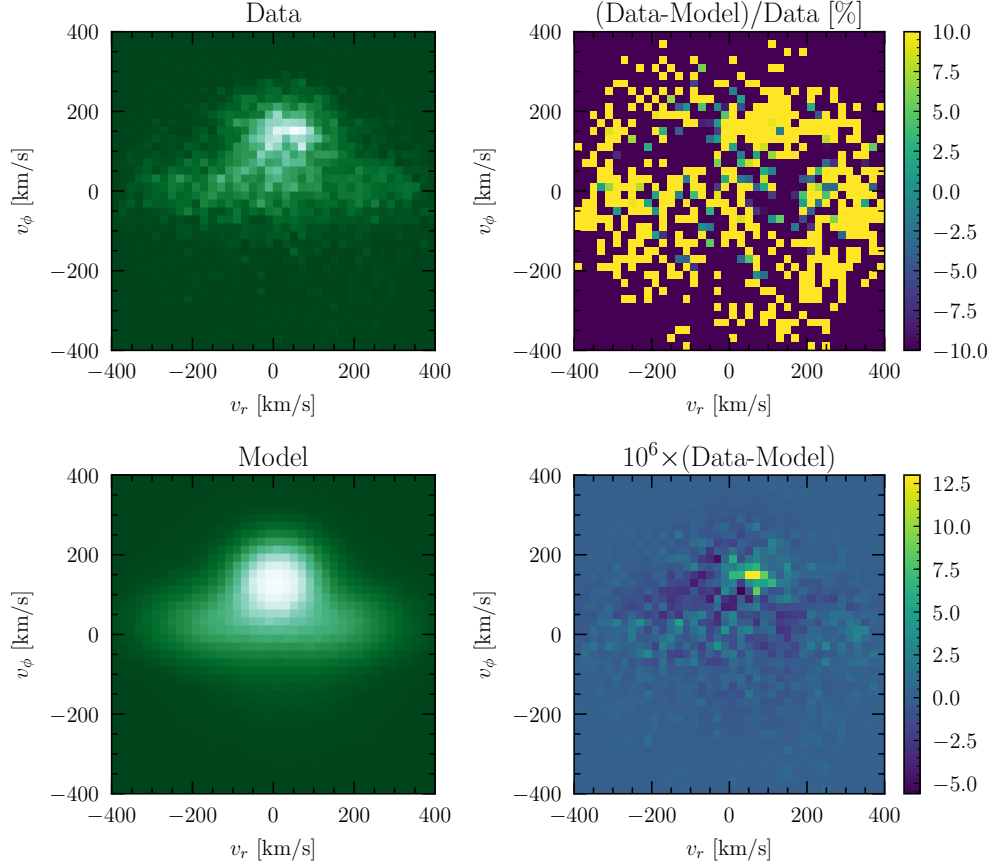


Figure S1. A comparison of the data and best-fit model distributions in the $v_r - v_\phi$ plane for the SDSS-*Gaia* DR2 data in the region $r \in [7.5, 8.5]$ kpc and $|z| > 2.5$ kpc. The left column shows a count map of the data (top) and model (bottom). The right column compares the two explicitly, showing the fractional (top) and total (bottom) residuals. The bottom right plot is the difference in the value of the binned histograms, where both the data and model are normalized to unity beforehand.

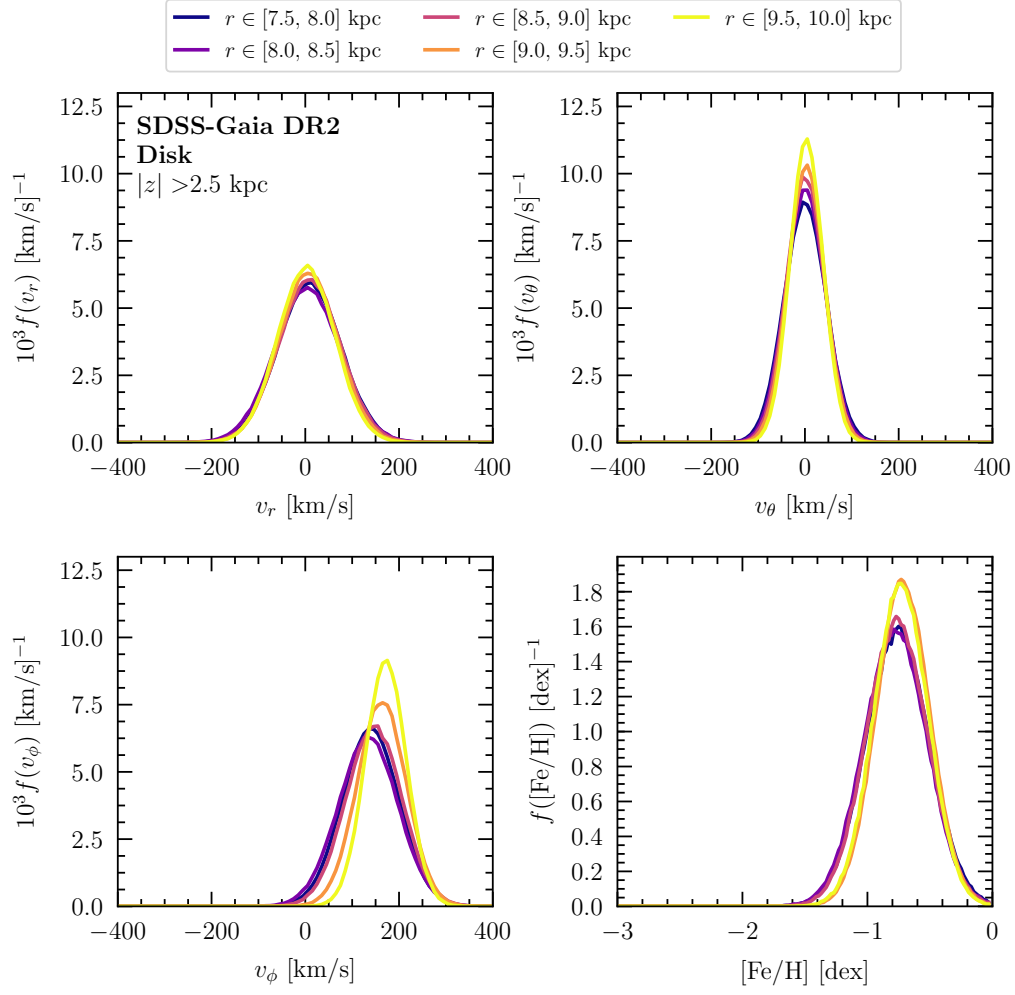


Figure S2. The same as Fig. 4, except for different radial cuts and fixing $|z| > 2.5$ kpc.

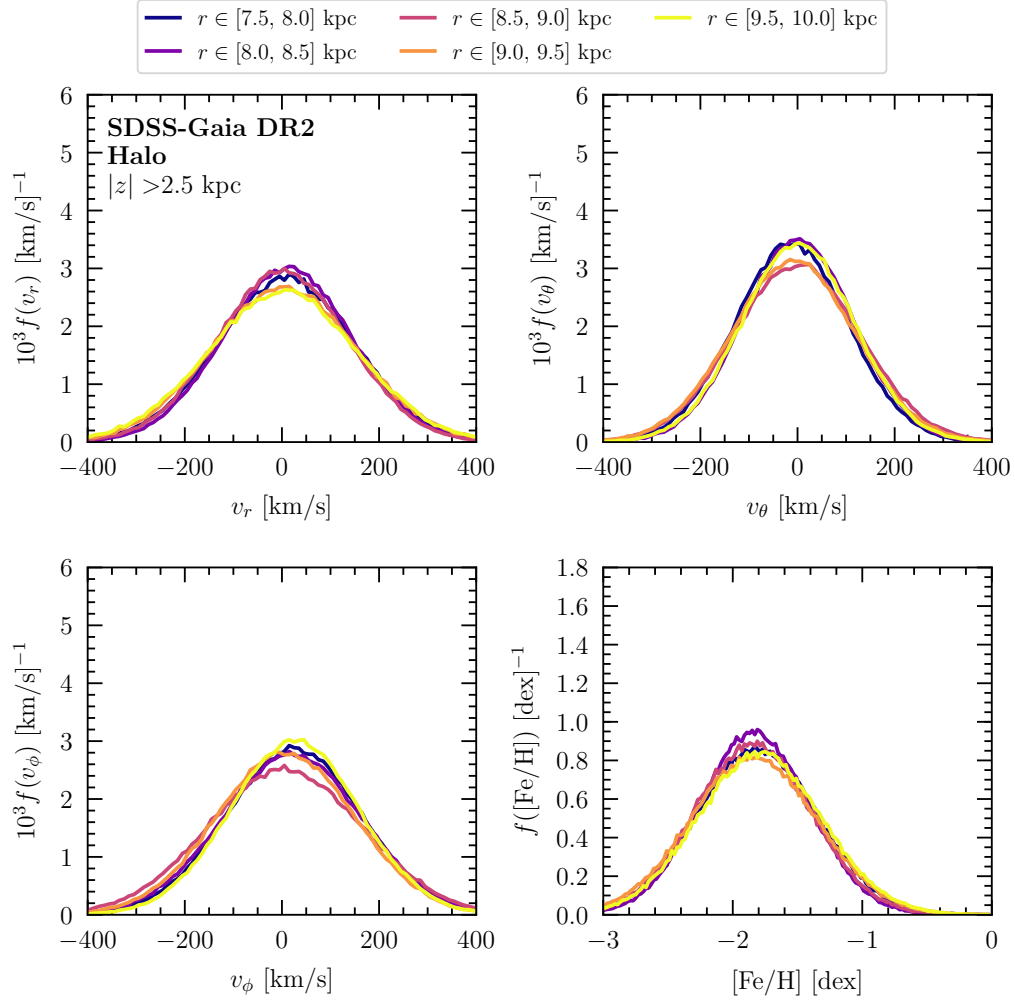


Figure S3. The same as Fig. 5, except for different radial cuts.

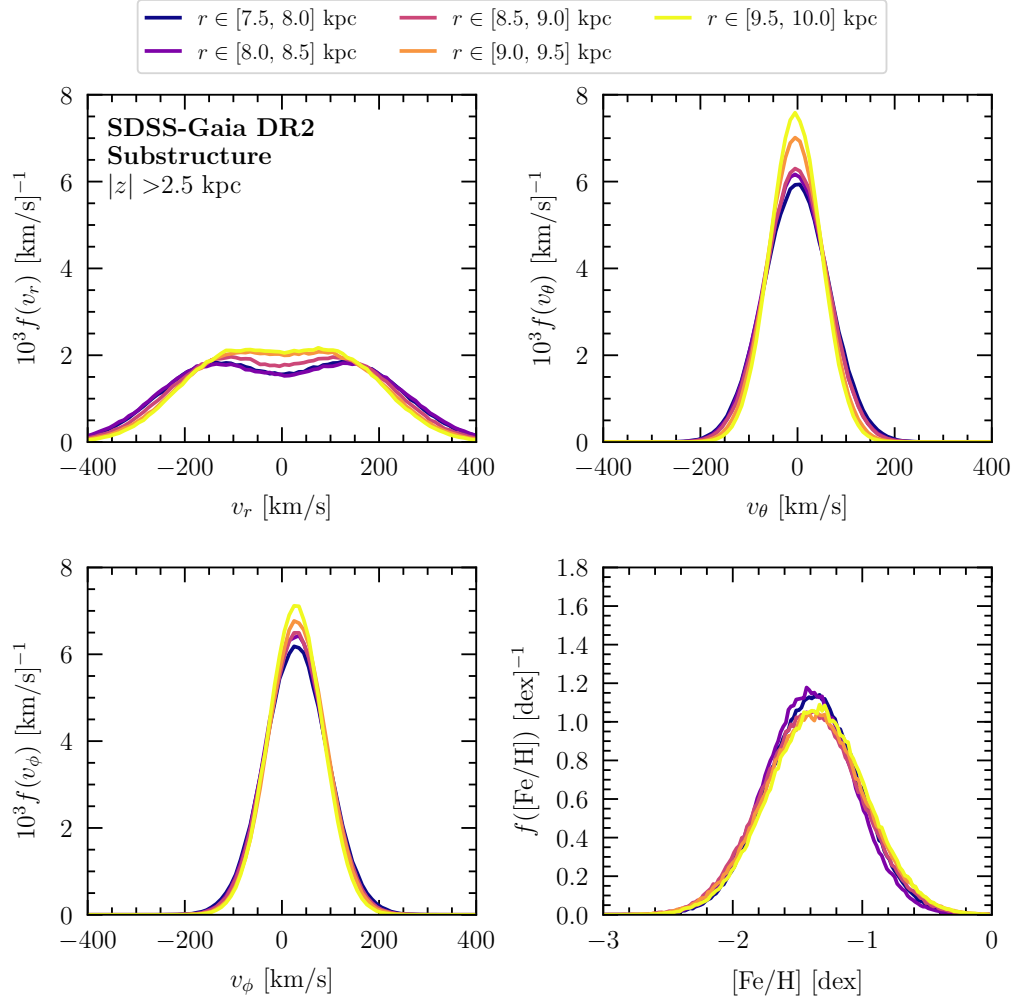


Figure S4. The same as Fig. 6, except for different radial cuts.

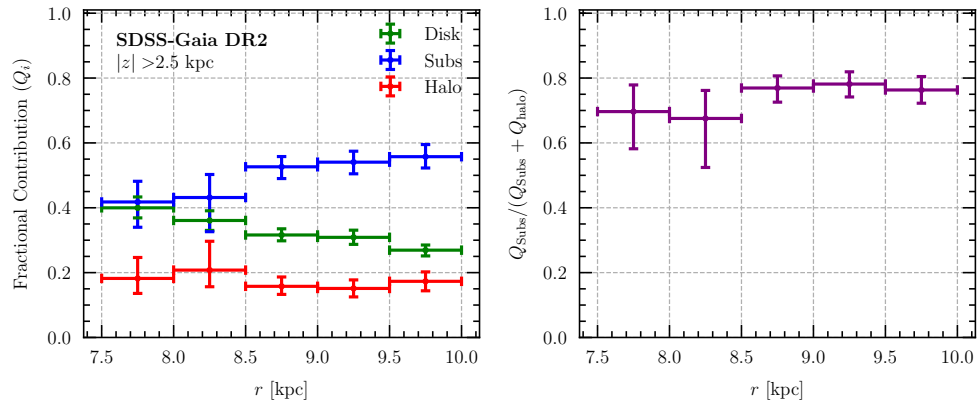


Figure S5. The same as Fig. 7, except for different radial cuts.